The Aeronautical Journal (2022), **126**, pp. 830–847
doi:10.1017/aer.2021.106

REGULAR PAPER

The smart morphing winglet driven by the piezoelectric Macro Fiber Composite actuator

X. Chen, J. Liu and Q. Li*

State Key Laboratory for Strength and Vibration of Mechanical Structures, School of Aerospace Engineering, Xi'an Jiaotong University, Xi'an, China
***Corresponding author.** Email: qunli@mail.xjtu.edu.cn

Received: 23 February 2021; **Revised:** 9 September 2021; **Accepted:** 18 October 2021

Keywords: Smart morphing winglets; Piezoelectric MFC; Intelligent MFC bending actuator; Finite element model

Abstract

A smart morphing winglet driven by piezoelectric Macro Fiber Composite (MFC) is designed to adjust cant angle autonomously for various flight conditions. The smart morphing winglet is composed of the MFC actuator, DC-DC converter, power supply, winglet part and wing part. A hinge is designed to transfer the bending deformation of intelligent MFC bending actuator to rotation of the winglet structure so as to achieve the adaptive cant angle. Experimental and numerical work are conducted to evaluate the performance of smart morphing winglet. It is demonstrated that the proposed intelligent MFC bending actuator has an excellent bending performance and load resistance. This smart morphing winglet exhibits the excellent characteristic of flexibility on large deformation and lightweight. Moreover, a series of wind tunnel tests are performed, which demonstrate that the winglet driven by intelligent MFC bending actuator produces sufficient deformation in various wind speed. At high wind speed, the cant angle of the winglet can reach 16 degrees, which is still considered to be very useful for improving the aerodynamic performance of the aircraft. The aerodynamic characteristics are investigated by wind tunnel tests with various attack angles. As a result, when the morphing winglet is actuated, the lift-to-drag ratio could vary up to 11.9% and 6.4%, respectively, under wind speeds of 5.4 and 8.5m/s. Meanwhile, different flight phases such as take-off, cruise and landing are considered to improve aerodynamic performance by adjusting the cant angle of winglet. The smart morphing winglet varies the aerofoil autonomously by controlling the low winglet device input voltage to remain optimal aerodynamic performance during the flight process. It demonstrates the feasibility of piezoelectric composites driving intelligent aircraft.

1.0 Introduction

Smart morphing aircraft is generally designed for specialised missions where smart materials and unique structures are often used [1–3]. To advance aerodynamic performance of aircraft, various approaches have been reported, especially using biomimetic, lightweight, adaptive and multifunctional materials and structures [4–6]. Meanwhile, induced drag is the main component of flying drag of the aircraft, which accounts for about 40% in cruise phase, and even reaches 50%–70% in takeoff and climbing phase [7]. Therefore, it is of great significance to reduce the induced drag during the flight of smart morphing aircraft.

The winglet is known to improve the aerodynamic efficiency and reduce the induced drag by diffusing wing-tip vortices on the wing edge [8]. The additional functionalities of winglets include yaw control and vertical stabilisation, as well as to improve efficiency [9]. However, all of the conventional winglets are designed only in the cruising state and fixed in the aircraft wings with the unchanged cant angle. The geometric parameters and layout of the winglets are optimised only for the cruise phase, while variable cant angle winglet can change the lift drag ratio of the wing and improve the aerodynamic performance of the aircraft [10]. It is imperative to design the morphing aircraft winglet benefiting in the whole

flying phase including take-off, climbing, cruise, etc. It is expected that the winglet with variable cant angle can change the geometry and parameters in real time, and provides the aircraft with optimal drag reduction effect throughout the whole flight envelope. For example, increasing the cant angle during take-off minimises induced drag and allows the aircraft to take off with less thrust. This can reduce energy consumption and vibration noise. When the aircraft reaches the cruising altitude, the winglet returns to the initial design state to optimise the resistance characteristics of the cruise phase.

The aircraft winglet has been studied for decades [11,12]. Most of existing methods of carrying morphing aircraft winglets are used rigid components, with joints, linkages, gears, and motors. Winglets with variable cant angles can even be used as aerodynamic rudder to control aircraft for roll and yaw manoeuvers [13]. Wang et al. [14] carried out conceptual study of a morphing winglet based on unsymmetrical stiffness. The morphing winglet has to change its cant angle, and its stiffness has to be large enough to carry loads. Bourdin et al. [15] investigated a novel method for the control of morphing aircraft. The concept consists of a pair of winglets with adjustable cant angle, independently actuated and mounted at the tips of a baseline flying wing. Arena et al. [16] carried out an aero-servo-elastic design of a morphing wing trailing edge system for enhanced cruise performance. Dimino et al. [17] addressed actuator integration aspects of a winglet shape-changing flight surface capable of adaptively enhancing aircraft aerodynamic performance and reducing critical wing structural loads. Breuker et al. [18] designed morphing winglets with the inclusion of nonlinear aeroelastic effects; it has been shown that morphing winglets can improve the performance of fixed winglets significantly for regional airliners. However, the conventional winglet is mainly composed of rigid components, with joints, linkages, gears, and motors, although the aircraft winglet systems can perform tasks with precise and articulated motion [19–26]. There are many disadvantages like heavy weight and requiring cost. Particularly, the complex integrated feedback-based control and driving systems are required to the conventional mechanical winglet.

Smart materials and structures play a significant role in the design of flexible morphing aircraft, without requiring additional mechanical components and complicated control systems [27–29]. The smart morphing aircraft winglet has developed by mimicking biological behaviour using smart materials, which can deform flexibly during actuation. Bilgen et al. [30] presented a completely piezoelectric controlled aircraft; a type of piezocomposite actuator was used for changing the camber of all control surfaces on the aircraft. Han et al. [31] investigated the aerodynamic performance of a self-contained morphing winglet for an unmanned aerial vehicle that mimics the wing-tip feathers of gliding birds. Various actuators made of smart materials have been used in the field of the smart aircraft, such as shape memory alloys (SMAs), shape memory polymers (SMPs), piezoelectric zirconate titanate (PZT) and piezoelectric Macro Fiber Composites (MFCs) [32–39].

It is emphasised that piezoelectric MFC as an excellent actuator was invented in 1996 by the National Aeronautics and Astronautics Administration (NASA) Langley Research Center. MFCs have been widely used in smart controllers, actuators, and sensors. MFCs provide accurate control and electromechanical signal conversion for intelligent actuator and sensor through its unique electromechanical coupling characteristics.

An innovative smart morphing winglet driven by MFC is proposed, inspired by the bionic ideas of the tip feathers of gliding birds. The smart morphing winglet consists of a power supply, DC-DC converter, MFC bending actuator winglet part and wing part. Intelligent MFC bending actuator is selected as the driving components of the winglet in this paper. By controlling the input voltage, the winglet driven by MFC bending actuator can perform soft and smooth rotational deformation to optimise the cant angle. The aerodynamic coefficients are measured using an open-blowing type wind tunnel testing for different angles of attack under low and high wind speeds. The winglet driven by intelligent MFC bending actuator can be continuously deformed by driving voltage for the different flight states of aircraft. This ensures that the aircraft always maintains the best aerodynamic performance during the whole flight process.

This paper is organised as follows: Section 2 provides the design method and characteristics of smart morphing winglet and MFC bending actuator. Section 3 illustrates the wind tunnel test and aerodynamic experiment of the smart morphing winglet device, and Section 4 is devoted to the conclusion.

https://doi.org/10.1017/aer.2021.106 Published online by Cambridge University Press

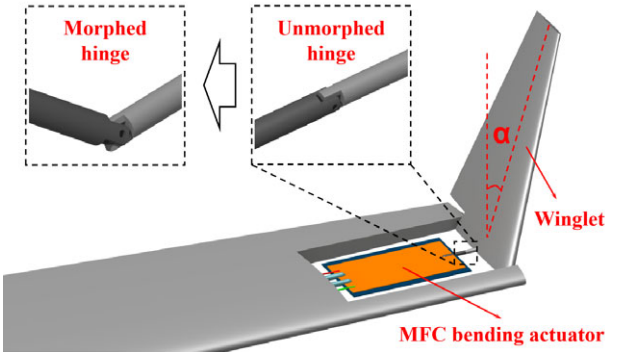

Figure 1. *A schematic diagram of the smart winglet driven by MFC bending actuator.*

2.0 The smart morphing winglet driven by mfc actuator

2.1. Concept

Here, we report on a novel smart morphing winglet actuating by intelligent MFC bending actuator. The smart morphing winglet device consists of the intelligent MFC bending actuator, a hinge, winglet part and wing part. The power supply and DC-DC converter are hidden in the wing part, and the angle between the winglet and the vertical is defined as the cant angle α, as shown in Fig. 1. The intelligent MFC bending actuator as a key component of smart winglet is designed. As a part of the winglet, a hinge shown in Fig. 1 is used, which transfers the deformation to create a smart morphing winglet that exhibits flexible rotational deformation with lightweight system.

This structure of undeformed and deformed smart morphing winglet are shown in Fig. 2(a) and (b). MFC bending actuator is flat with no voltage input. Then the MFC induced by the driving voltage with its electro-mechanical coupling characteristics, which results in the bending deformation of the substrate, enabling the winglet to achieve significant rotating motion with the slippage of the MFC bending actuator along the wing, as shown in Fig. 2(b). The cant angle can be varied depending on the driving of intelligent MFC bending actuator in the winglet. The length of the short handle s and the bending height of the MFC bending actuator y are shown in the Fig. 3(a) and (b), then the change of the cant angle $\Delta\alpha$ can be obtained by Equation (1).

$$\Delta\alpha = \arcsin\frac{y}{s} \tag{1}$$

The rotating performance of the winglet is evaluated to determine the optimal design, considering the response time and the driving force. The advantage of the proposed design is to increase winglet flexibility with less increase in the induced drag force and weight of the aircraft during the various flight conditions. The movement of the actuator can be changed by varying the position and the orientation of the MFCs. Moreover, multi-dimensional motion like spanswise and chordwise bending can be achieved by controlling the arrangement of the MFCs, which can mimic complex biological behaviour.

2.2. MFC bending actuator

2.2.1 Experiment of MFC bending actuator driven by DC voltage

Several tests and simulations are carried out to evaluate the bending capability of the MFC bending actuator with various thickness and elastic modulus of the substrate, including response time and bending force tests.

The intelligent MFC bending actuator is fabricated with the following dimensions: a matrix with 100mm length, 36mm width, and 0.2mm thickness, and a M-5628-P1 MFC supported by Harbin Core Tomorrow Science & Technology as shown in Fig. 3. The "P1" of M-5628-P1 MFC indicates that

https://doi.org/10.1017/aer.2021.106 Published online by Cambridge University Press

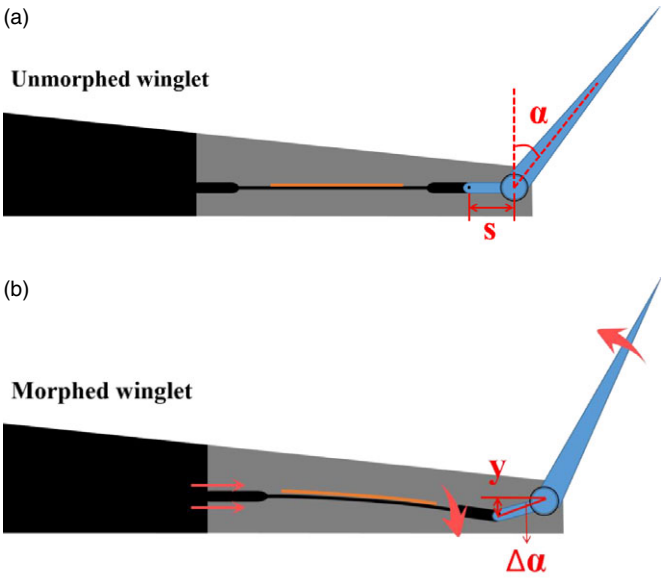

Figure 2. *A schematic diagram of the flexible motion of winglet; (a) unmorphed winglet (b) morphed winglet, where* α *denotes the cant angle.*

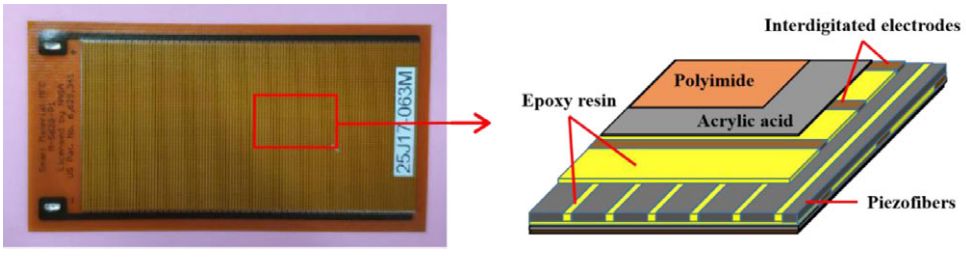

Figure 3. *Schematic diagram of MFC used in the winglet structure.*

it is an elongating MFC, which utilises the d_{33} effect for actuation. Here, the MFC comprises three parts—a piezoelectric ceramic fiber layer, an interdigitated electrode and a polymer matrix. MFCs use interdigitated electrodes to apply a uniform voltage along the length of the piezoelectric fibers, thereby making them contract or extend depending on the voltage potential.

An experiment is proposed to characterise the MFC bending actuator. The schematic diagram of its driving circuit is shown in Fig. 4(a), where R_0 is a resistor used to accelerate the recovery deformation of MFC bending actuator. The DC-DC converter device can transfer the low voltage (0–5V) of power supply to high voltage(0–1,500V) with low weight, small size, and the power only 0.33W, as shown in Fig. 4(b). Low voltage of power supply input in DC-DC converter is converted into high voltage to drive MFC. As shown in Fig. 5, one side of the MFC bending actuator is fixed by the magnetic generator. The end of the substrate is illuminated by a laser displacement meter to show its maximum deflection.

The signal generator transmits low voltage to the converter. When the driving voltage converted by DC-DC converter is applied, there will be a deflection at the end of the MFC bending actuator, and the deformation will be restored when the voltage is removed. The resistor will accelerate the recovery stroke when the high voltage is removed. The output voltage, end deflection of the MFC bending actuator and time to recovery deformation are different because of the different of resistance.

https://doi.org/10.1017/aer.2021.106 Published online by Cambridge University Press

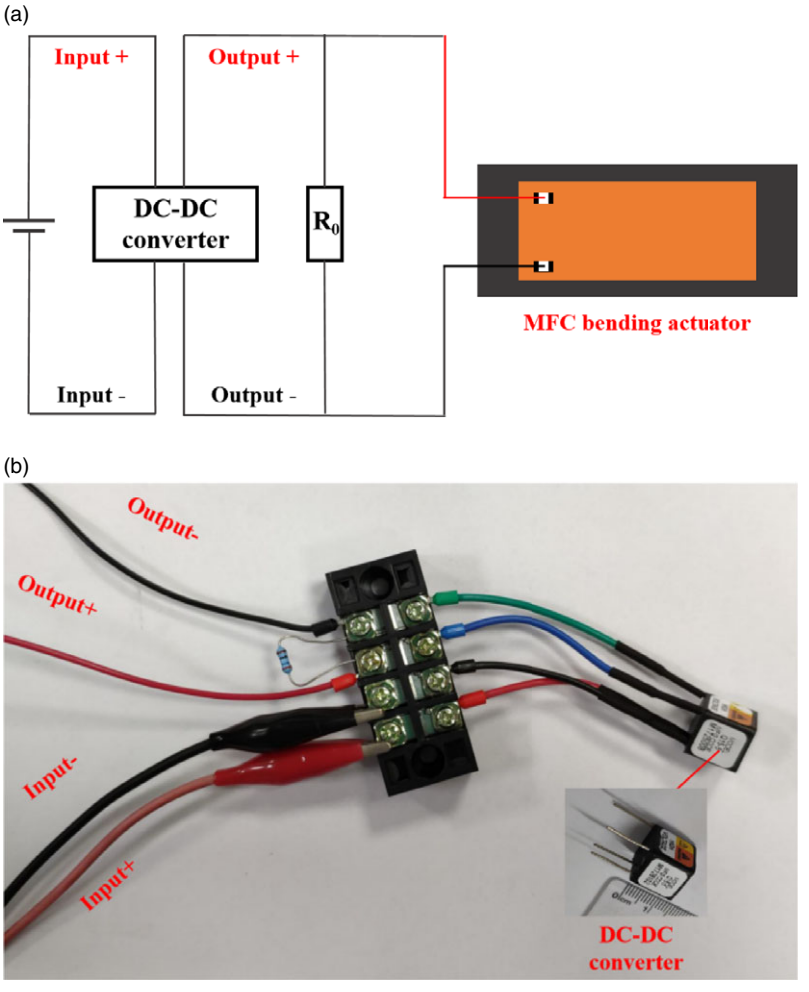

Figure 4. *Circuit of the MFC actuating test; (a) diagram of the circuit, (b) the DC-DC converter.*

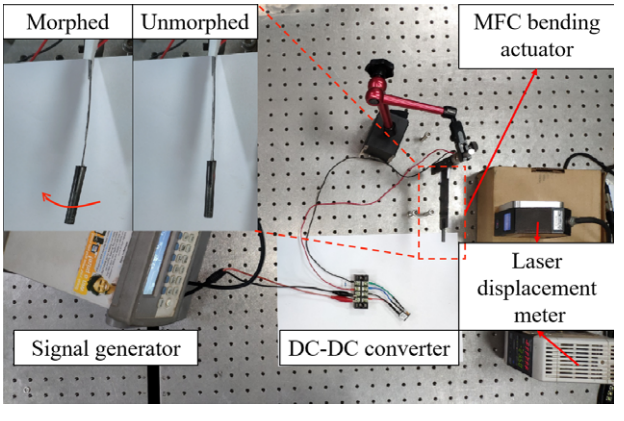

Figure 5. *The actuation test of MFC bending actuator.*

https://doi.org/10.1017/aer.2021.106 Published online by Cambridge University Press

Table 1. *The relationship of the output voltage, deflection of the MFC bending actuator and time to recovery deformation with of varied resistance value*

Resistance Value (MΩ)	**Output Voltage (V)**	**Deflection (mm)**	**Time t_1(s)**
10	677	3.6	0.1
20	680	4	1.0
30	684	4.2	2.5
40	672	4.3	4.0
100	644	4.3	6.0

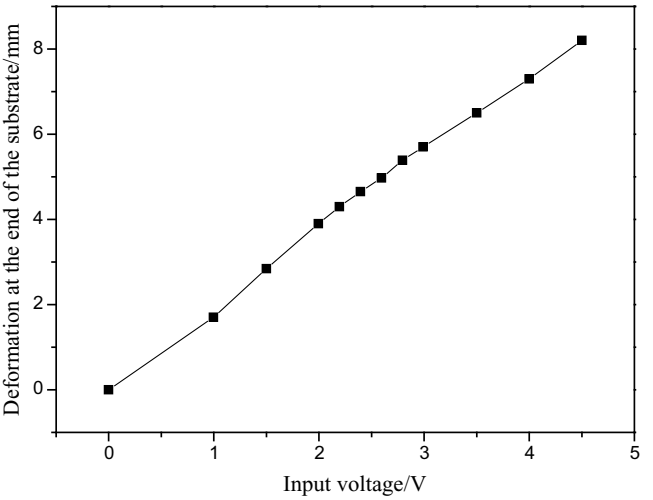

Figure 6. *The deflection of the end of the substrate and the input voltage.*

The input voltage is set to 2.5V. The results are shown in Table 1; with the increase of resistance value, the output voltage first increases and then decreases, and the end deflection and recovery time gradually increase. When the resistance is 20MΩ, the deformation is still 4mm, and it only takes one second to recover its deformation. In this paper, 20MΩ is considered as the optimum resistance which can accelerate the recovery deformation without affecting the driving displacement of the MFC bending actuator in this actuation test.

Figure 6 shows the deformation of the intelligent MFC bending actuator induced by a DC voltage. The driving voltage is continuously applied to the actuator till reaching the maximum deformation. As shown in Fig. 6, the end deflection of the steel sheet varies linearly from 0 to 7.9mm when the input voltage from 0 to 5V, which supplies sufficient motion to actuate the rotation motion of the smart morphing winglet. The bending deflection of the intelligent MFC bending actuator varies smoothly, which is an important aspect of the morphing performance of the winglet.

2.2.2. Simulation and optimisation of the MFC bending actuator

The efficiency of the designed smart morphing winglet driven by the MFC actuator needs to be predicted more efficiently by the finite element method. Therefore, an electro-mechanical finite element model is developed to simulate the deformation behaviour of the proposed MFC bending actuator.

MFC is a kind of inhomogeneous composite. It illustrates that the electrodes and piezoelectric fibers play a major actuating role in it, so the effective elastic modules and piezoelectric parameters of MFC

https://doi.org/10.1017/aer.2021.106 Published online by Cambridge University Press

Table 2. *Effective material parameters of the equivalent M-5628-P1 MFC*

Parameter	Value	Equivalent Elastic Modulus	Value (Pa)
Thickness	0.3mm	e_{11}	4.286×10^{10}
Length	56mm	e_{12}	7.176×10^{9}
Width	28mm	$e_{13}= e_{23}$	7.433×10^{9}
Maximum output displacement	0.108mm	e_{22}	1.973×10^{9}
		e_{33}	3.222×10^{10}
Maximum output force	450N	$e_{44}=e_{55}$	6.99×10^{9}
Equivalent piezoelectric constant d_{33}	5.07×10^{-8}m/V	e_{66}	7.183×10^{9}

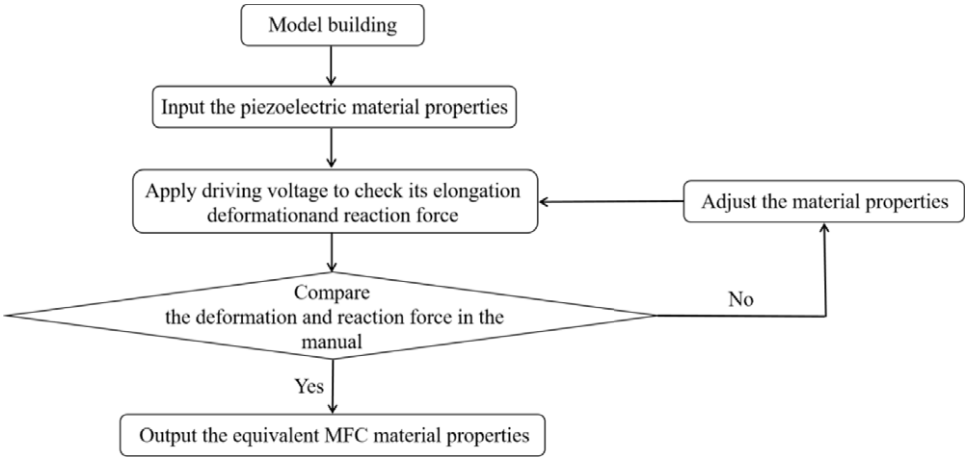

Figure 7. *Flowchart of FEM implementation procedure of the equivalent MFC material properties.*

are used to simplify the MFC as a homogenous body in the numerical process. The handbook supported by Harbin Core Tomorrow Science & Technology states that the active area of the M-5628-P1 MFC is 56mm in length by 28mm in width. And the thick of the MFC actuator is 0.3mm. The maximum displacement (0° fiber direction) of MFC is 0.108mm under maximum driving voltage of −500–1,500V input on the negative and positive electrodes of MFC, respectively, and the maximum output force is 450N at a driving voltage of 0–1,500V.

The equivalent M-5628-P1 MFC finite element model is established based on the results of the maximum displacement and output force obtained from the product manual. As shown in Fig. 7, the initial piezoelectric constants and elastic modulus of a common piezoelectric material are inputted to obtain the original elongation deformation and the original reaction force. Then comparing the elongation deformation and reaction force data in the manual, the piezoelectric material properties and elastic modulus are continuously adjusted until they match the elongation deformation and reaction force in the product manual. Therefore, the equivalent MFC material properties derived from this process are given in Table 2, the equivalent piezoelectric constant d_{33} and elastic modulus are included. In this case, the mechanical and electrical properties of the equivalent MFC finite element model are consistent with the parameters of the product manual.

This behaviour is simulated using finite element method and verified by the MFC actuation test. Figure 8(a), (b) and (c) shows the model, mesh, and displacement contour plot of the MFC bending actuator, respectively. The deformation of the MFC bending actuator is uniform and the maximum

https://doi.org/10.1017/aer.2021.106 Published online by Cambridge University Press

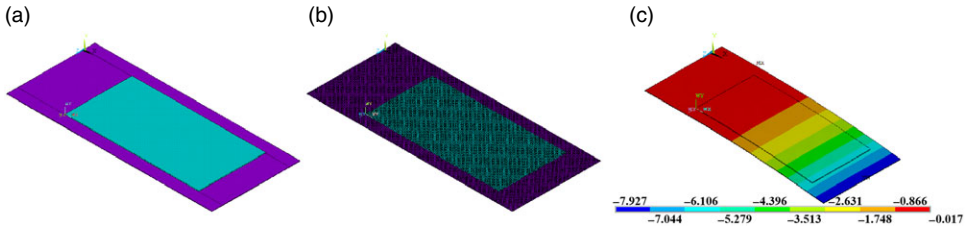

Figure 8. *Numerical simulation of the MFC bending actuator; (a) FEM model, (b) FEM mesh, (c) displacement contour plot (unit: mm).*

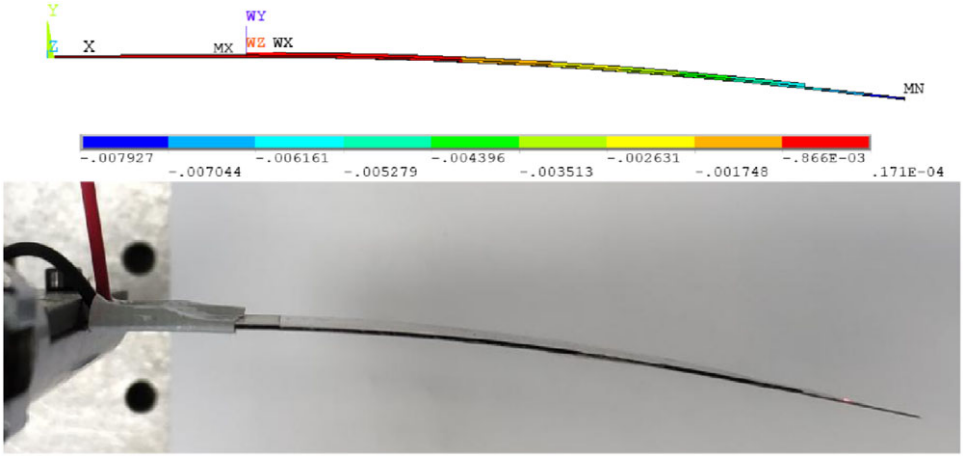

Figure 9. *Deformation of the MFC bending actuator under the finite element method and the test.*

deflection is 7.9mm at the end of the substrate. The comparison between the finite element model and deformation of the MFC bending actuator in the experiment is shown in Fig. 9. It is concluded that the form of deformation is consistent with the result. As shown in Fig. 10, the end deflection of the steel sheet varies linearly from 0 to 7.9mm when the driving voltage varies from 0 to 1,500V, which is consistent with the results from the test of the MFC bending actuator.

Through the equivalent finite element model of piezoelectric MFC, it can provide reference for the selection of the type of the piezoelectric materials, actuating substrate thickness, elastic modulus, and optimising the actuating effect and actuating force of the MFC bending actuator conveniently. After the effective material parameter of the MFC is obtained, numerical simulations are carried out to derive the cant angle of winglet under different elastic modulus and the thickness of the substrates. The optimised size and materials of the intelligent MFC actuator are demonstrated by a series numerical calculation. Figure 11 shows the relationship of the maximum end-edge deflection and the elastic modules, thickness of the substrate. The result shows that the driving deflection of intelligent MFC bending actuator decreases with the increase of the elastic modulus and the thickness of the substrate. At the same time, the thinner the substrate is, the greater the deformation capacity is, but the ability to resist wind load is also weakened. In order to meet the requirement of motion and load resistance of the winglet driven by intelligent MFC bending actuator in this paper, a 65-Mn steel with elastic modulus 210GPa and the thickness of matrix 0.2mm is used to construct the winglet, and the maximum deflection of the actuator can reach 10.4mm.

https://doi.org/10.1017/aer.2021.106 Published online by Cambridge University Press

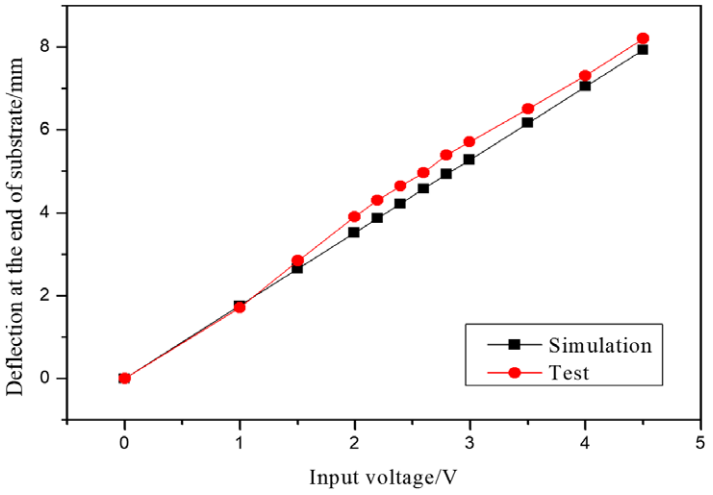

Figure 10. *The relationship between the deflection of the end of the substrate and the input voltage by simulation and test.*

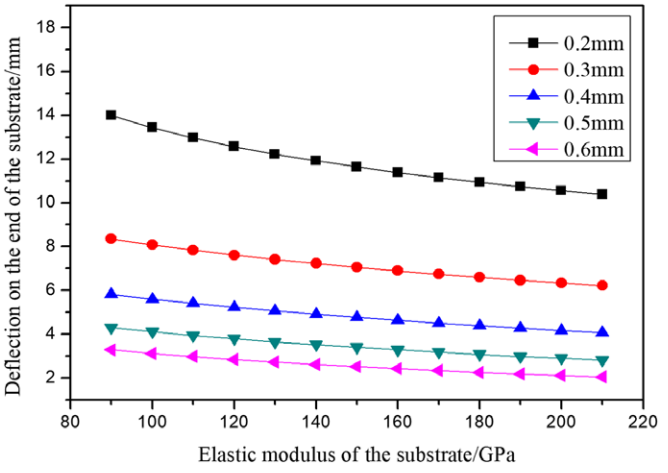

Figure 11. *Maximum end-edge deflection as a function of the elastic modules and thickness (0.2–0.6mm) of the substrate.*

3.0 Apparatus of smart morphing winglet and wind tunnel test

3.1. Initial experiment of the smart morphing winglet

As shown in Fig. 12, the winglet consists of MFC bending actuator, wing part, and winglet part. While wing part with length of 180mm and width of 25mm is fabricated by light wood and plastic film. The winglet part with length of 140mm is made of foam wrapped by carbon fiber, the geometry size of the winglet with symmetrical streamline areofoil is shown in Fig. 13. MFC bending actuator and the hinge are built into the wing part. All connections are made of carbon fiber tubes.

An experiment is proposed to characterise the morphing performance of the winglet driven by intelligent MFC actuator. The signal generator, DC-DC converter, fixture and angle calibration paper are introduced to operate the actuation test of smart morphing winglet. The driving voltage converted from the input voltage of the power supply to high voltage by the DC-DC converter is continuously applied to the smart morphing winglet till reaching the maximum deformation. The morphing performance with an input voltage in the range of 0–5V is analysed using an angle calibration paper. Figure 14 shows the

https://doi.org/10.1017/aer.2021.106 Published online by Cambridge University Press

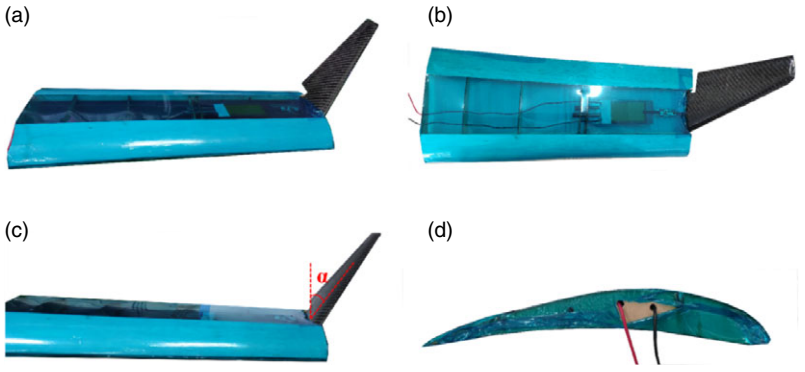

Figure 12. *The winglet driven by the intelligent MFC actuator; (a) stereo view, (b) top view, (c) front view, (d) aerofoil view.*

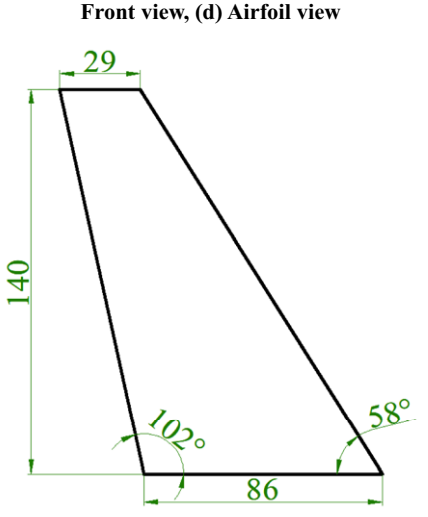

Figure 13. *Geometry size of the winglet (unit mm).*

bending angle as a nearly linear relationship of the input voltage. The cant angle of the winglet increases smoothly from 43° to 20° as the input voltage varies from 0 to 5V. The cant angle of the winglet varied smoothly with the driving voltage, which is an important part of the morphing performance. The winglet exhibits highly compliant rotating performance in the actuation test. Figure 15 shows a series of images illustrating the actuation sequence of the smart morphing winglet driven by intelligent MFC actuator with an input voltage of 0–5V. The experimental results show that it is feasible to drive the structure of the aircraft by controlling the intelligent materials with low input voltage.

3.2. Wind tunnel test of the smart morphing winglet

Under different wind speeds, the cant angle of the winglet will change due to the change of wing tip vortex on the wing. Investigation on the properties of the smart morphing winglet driven by intelligent MFC actuator under wind load is essential. The maximum range of the cant angle of the winglet is measured with different wind speeds. The deformation capability of the smart morphing winglet influenced by the aerodynamic force is measured in a wind tunnel. Experiments are carried out in an open-blowing type wind tunnel, as shown in Fig. 16. The dimension of the wind tunnel in the test section is 50cm × 50cm,

https://doi.org/10.1017/aer.2021.106 Published online by Cambridge University Press

Table 3. *Dimensions and parameters of the wind tunnel test*

Parameter	Value
Wing span	39 cm
Average chord length	14.5 cm
Wind tunnel	50×50 cm
Wind speed	4.5–8.5 m/s

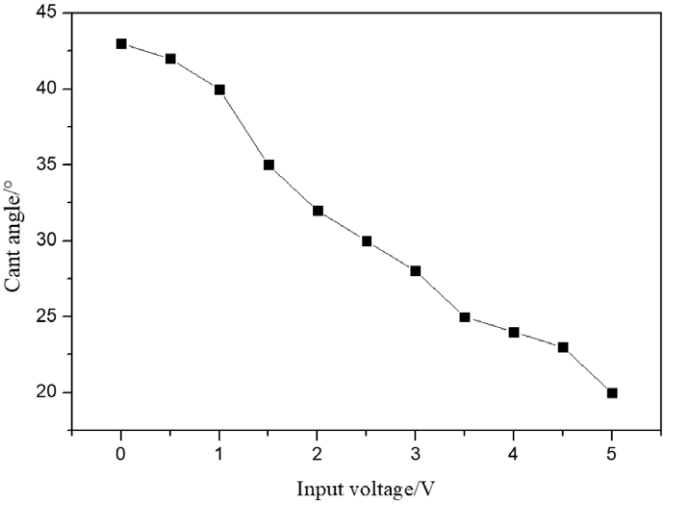

Figure 14. *The relationship of the cant angle and the input voltage.*

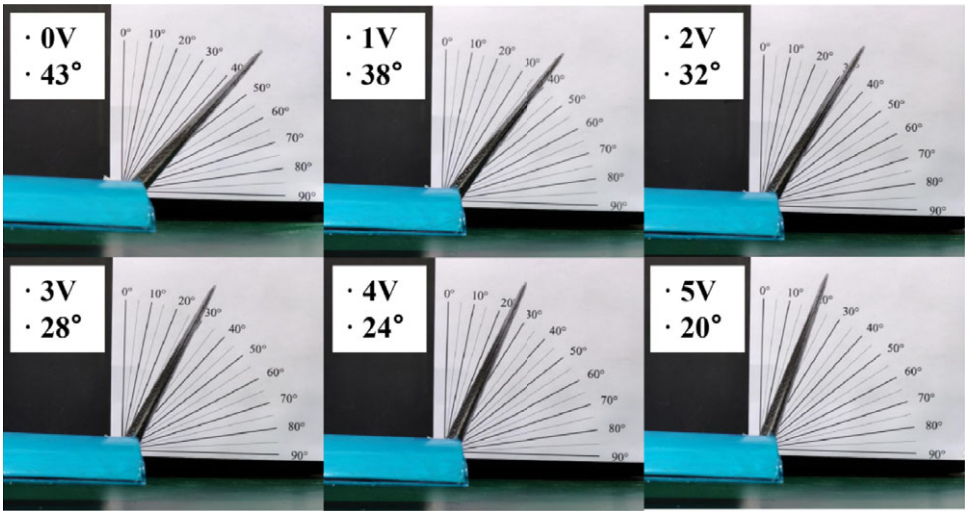

Figure 15. *The cant angle of the winglet driven by the different input voltage.*

the wind speeds varied from 4.47 to 8.46m/s by regulating the frequency of fans. The wind blows in the direction of the wing, and the input voltage is provided by a signal generator. The winglet is clamped to the right of the wind tunnel. The range of the varied cant angle can be measured under different wind speeds from 4.47 to 8.46m/s. The relevant parameters utilised in the wind tunnel experiment are listed in Table 3.

https://doi.org/10.1017/aer.2021.106 Published online by Cambridge University Press

Table 4. *The relationship between wind speed and the range of the cant angle with the input voltage from 0 to 5V*

Wind Speed v_m (m/s)	The Winglet Cant Angle Without Input Voltage (°)	The Winglet Cant Angle At 5v Input Voltage (°)
4.47	45	26
5.48	43	25
6.45	40	23
7.44	37	20
8.46	33	17

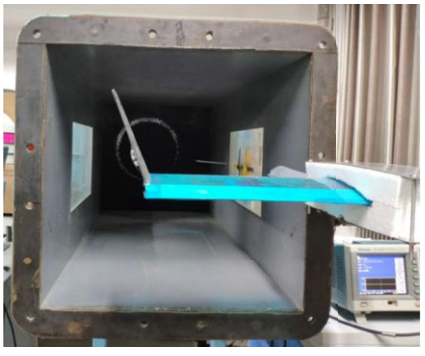

Figure 16. *Wind tunnel test setup of smart morphing winglet.*

The wind speed v_m, winglet cant angle without input voltage and the winglet cant angle at maximum input voltage of 5V is measured by wind tunnel tests. As shown in Table 4, the variation range of the cant angle exhibits slight effects for the low wind speed, i.e. v_m<5.0m/s and exhibits varying degrees effect for the high wind speed, i.e. v_m>5.0m/s. The control capability of intelligent MFC bending actuator to the smart morphing winglet decreases with the increase of wind speed. At high wind speed, i.e. 8.46m/s, the variation range of the cant angle of the winglet is also 16 degrees, which is still considered to be very useful for improving the aerodynamic performance of the aircraft [40–42]. Based on these wind tunnel tests, we can conclude that the variable range of cant angle of the winglet brought by the MFC bending actuator can effectively improve the flight efficiency of the aircraft. Hence, it is possible to realise a biomimetic winglet structure using the intelligent MFC bending actuator to realise the wing shape adjustment for different tasks under different wind speeds.

3.3. Aerodynamic performance experiment of the smart morphing winglet

The ability of the morphing winglets to control aerodynamic performance at different angles of attack and different wind speeds was tested. Experiments are carried out in an open-blowing type wind tunnel under low and high wind speeds and the angle-of-attack is varied from 2° to 12° with an increments of 1°. The coordinate system is defined as follows: the positive X-axis is in the streamwise direction, the Y-axis is in the vertical direction, and the Z-axis is in the spanwise direction, with the origin was at the root of the winglet, as shown in Fig. 17. The winglet is attached to the wind tunnel, and a load cell for measuring the lift and drag of the airflow is connected to the root of the winglet through a clamping device. The load cell is placed outside of the wind tunnel test section. The dimensions of the test section of the wind tunnel are 0.6m×0.6m. The wind speeds for the testing are 5.4 and 8.5m/s, respectively, which represent the wind speeds of small UAV in take-off and landing phase and cruise phase, respectively.

https://doi.org/10.1017/aer.2021.106 Published online by Cambridge University Press

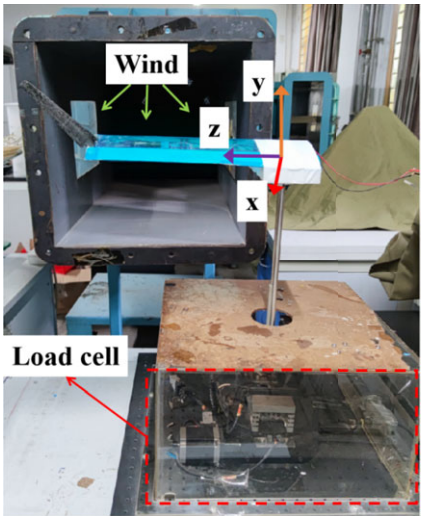

Figure 17. *A schematic diagram of the setup of the aerodynamic performance experiment.*

The coefficients of the lift and drag forces were calculated as follows:

$$C_{L,D} = \frac{F_{L,D}}{0.5\rho U_1^2 A} \tag{2}$$

where L is the lift force, D is the drag force, ρ is the density of air, U_1 is the wind speed, and A is the reference area. In this paper, the reference area A is the projected area of the wing, which is 0.075m^2. Figure 18(a) shows the drag coefficients as a function of the angle-of-attack under low wind speed. As the angle-of-attack increases, the drag coefficients become steadily larger for both cases of device input voltage being 0 and 5V. The results show that the winglet has a larger drag coefficient in the case of the device input voltage being 5V. By actuating the morphing winglet, the drag coefficients of the winglet vary by 2.7%–3.7%, which is obtained by comparing the varied value of drag coefficient before and after applying voltage with that before applying voltage, and the maximum difference is 3.7% at $\theta = 11^\circ$. Figure 18(b) shows the lift coefficient as a function of the angle-of-attack under low wind speed, which increases as the angle-of-attack increased. The winglet exhibits a larger lift coefficient in the case of the device input voltage being 5V.

The lift-to-drag ratios (L/D) calculated from the lift and drag coefficients of the winglet for the different angles of attack under low wind speed are shown in Fig. 18(c). The results show that the winglet with the device input voltage being 5V exhibits better performance. Especially when the angle-of-attack is less than 5°, the difference of the lift-to-drag ratio between the applied voltage of 0 and 5V is obvious. The largest lift-to-drag ratio occurs at $\theta = 2^\circ$ for both cases. The largest difference between cases of device input voltage being 0 and 5V occurs at $\theta = 3^\circ$, in which the morphed winglet with the device input voltage being 5V shows an L/D approximately 11.9% greater than the case of 0V.

Figure 19(a), (b) and (c) shows drag coefficients, lift coefficient and lift-to-drag ratio as a function of the angle-of-attack under high wind speed, respectively. By actuating the morphing winglet, the drag coefficients of the winglet vary by −2.2% to −6.4% in comparison with the initial geometry, and the maximum difference is 6.4% at $\theta = 2^\circ$. The winglet with device input voltage being 5V exhibits a larger lift coefficient expect $\theta = 7^\circ$. The largest difference is 4.8% between the two cases which occurred at $\theta = 12^\circ$. For lift-to-drag ratio, in which the winglet shows an L/D approximately 6.4% greater than the unmorphed wingtip. Meanwhile, the lift coefficient and drag coefficient increase with the increase of attack angle, but the lift drag ratio decreases with the increase of attack angle.

As shown in Figs 18 and 19, in the wind tunnel tests, the L/D of the winglet is strongly affected by the angle-of-attack. However, the smart morphing winglet with variable cant angle can control the lift drag

https://doi.org/10.1017/aer.2021.106 Published online by Cambridge University Press

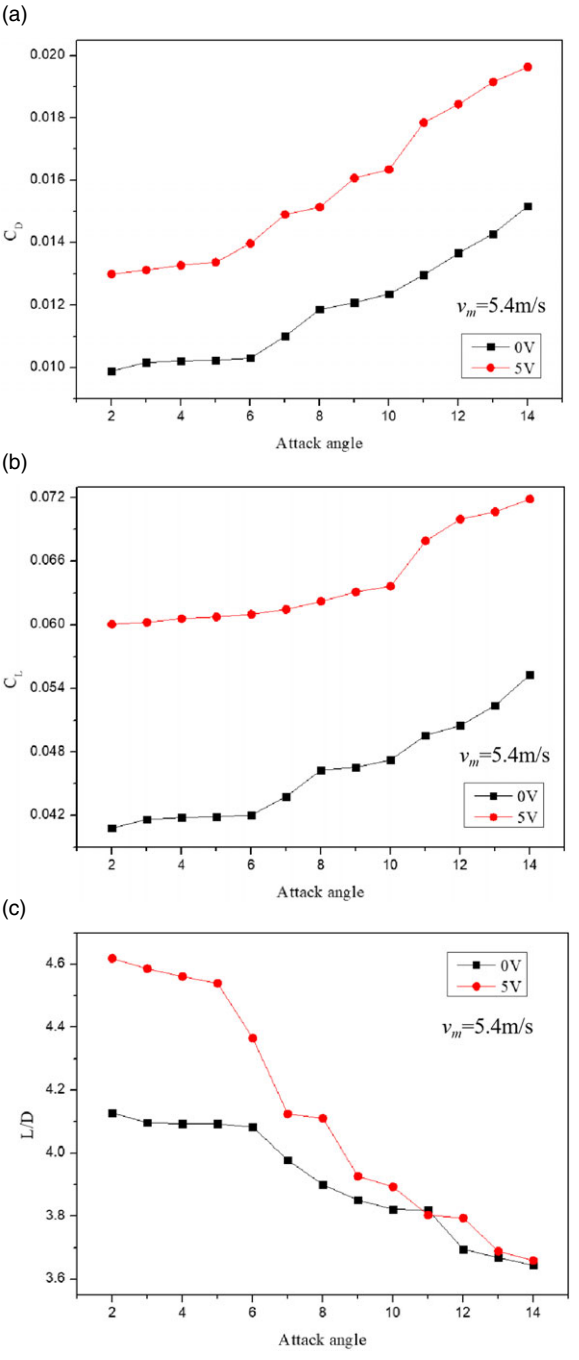

Figure 18. *Wind tunnel test results as a function of the angle-of-attack under low wind speed (5.4m/s); (a) drag coefficient (b) lift coefficient (c) lift-to-drag ratio.*

ratio of aircraft under different attack angles and wind speeds by adjusting the input voltage. The morphing winglet driven by intelligent MFC bending actuator provides potential for enhanced aerodynamic performance based on the cant angle of the winglet.

https://doi.org/10.1017/aer.2021.106 Published online by Cambridge University Press

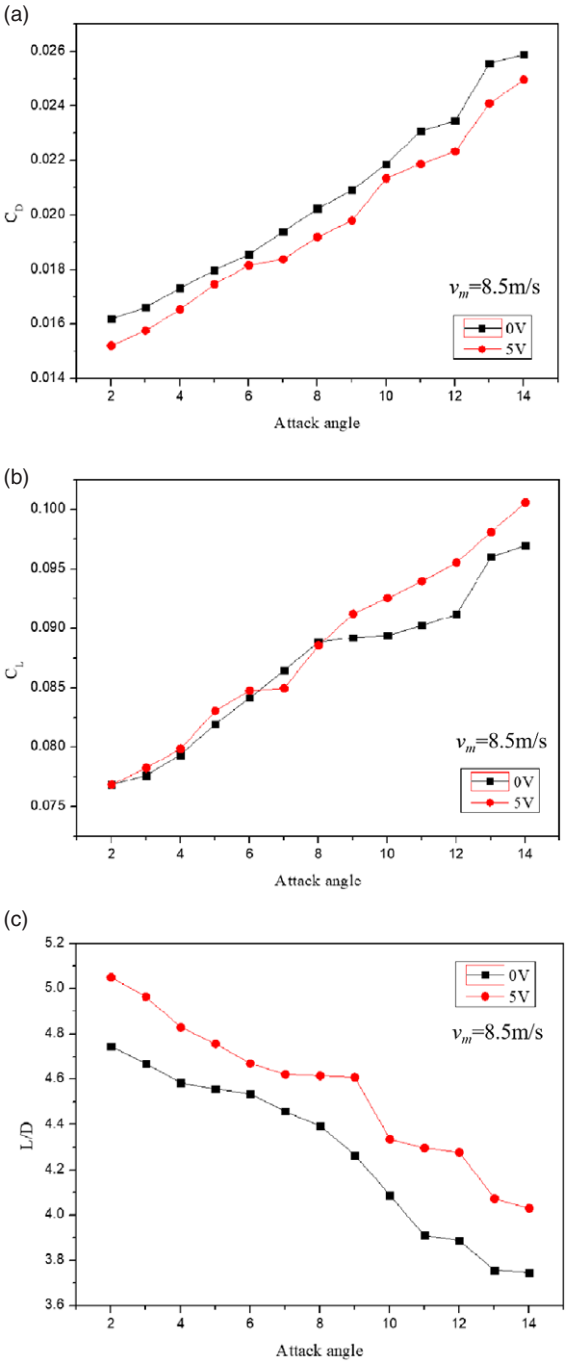

Figure 19. *Wind tunnel test results as a function of the angle-of-attack under high wind speed (8.5m/s); (a) drag coefficient (b) lift coefficient (c) lift-to-drag ratio.*

Based on these wind tunnel tests, we can conclude that the efficiency of the aircraft is able to be enhanced through the use of the smart morphing winglet. As shown in Fig. 20, low flight speed of the aircraft exists in takeoff and landing phase. The small cant angle winglet should be considered for takeoff

https://doi.org/10.1017/aer.2021.106 Published online by Cambridge University Press

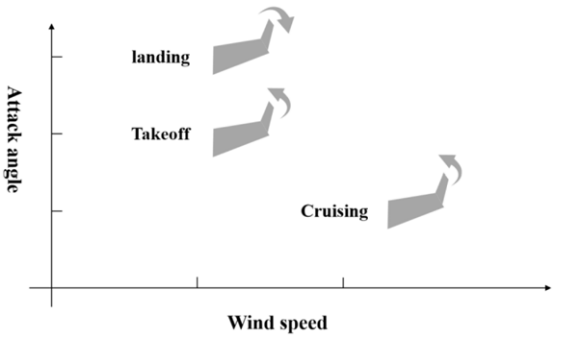

Figure 20. *Driving behaviour of winglet under different wind speeds and attack angles.*

stages with attack angle of about 5 degrees, while large cant angle winglet should be considered for landing stages with attack angle of about 10 degrees. Meanwhile, high flight speed of the aircraft with attack angle of about 0 degrees exists in cruise phase. In this case, small cant angle winglet should be considered for cruise stages. Therefore, the smart morphing winglet provides the scope to regulate the aerodynamic performance by choosing optimal wing geometry. By selecting the shape of the winglet considering the flight angle and speed, smart morphing winglets mounted on an aircraft show a better performance in comparison to an aircraft with fixed winglets, which further verifies the feasibility of piezoelectric smart material driving intelligent aircraft to complete the real-time adjustment of aerodynamic performance.

4.0 Conclusion

In this study, a smart morphing winglet with variable cant angle is developed using the intelligent MFC bending actuator. The apparatus is designed to optimise the aerodynamic efficiency for a wide range of flight conditions. Through the integrated winglet design, the reliable morphing of the cant angle could be acquired with smoothly sufficient deformation and control force and rapid response time of the intelligent MFC bending actuator. The cant angle of smart morphing winglet driven by intelligent MFC bending actuator can vary a range of 23° rapidly when the driving voltage of the winglet device increases from 0 to 5V. In high wind speed, the angle MFC actuator can reach 16 degrees, which is still considered to be very pivotal for improving the aerodynamic performance and flexibility of the aircraft. Meanwhile, the lift-drag-ratio of the winglet can be varied by up to 11.9 and 6.4% respectively under the wind speeds of 5.4 and 8.5m/s. The aerodynamic results of the lift-drag-ratio of the low wind speed and high wind speed to different attack angles show that the appropriate cant angle of the winglet can be adjusted by the lift-drag-ratio, attack angle, wind speed and other external environmental factors when the aircraft performs different tasks. Therefore, it is feasible that the adaptive morphing aircraft with smart materials to optimise aerodynamic performance in different flight stages. The future work will better combine the flexibility of piezoelectric smart materials with the compliant deformation of the structure, and a control procedures can be given to complete the control of real-time adjustment from electrical signal to the cant angle of winglet.

Acknowledgements. This work was supported by the National Natural Science Foundation of China (Nos.11772245), the Fundamental Research Funds for the Central Universities in China, and the Natural Science Basic Research Plan in Shaanxi Province of China (Program No. 2018JC-004). In addition, the author Qun Li gratefully acknowledges the support of K.C. Wong Education Foundation.

References

[1] Li, D., Zhao, S., Ronch, A.D., Xiang, J., Drofelnik, J., Li, Y., Zhang, L., Wu, Y., Kintscher, M. and Monner, H.P. A review of modelling and analysis of morphing wings, *Prog. Aerosp. Sci.*, 2018, **100**, pp 46–62.

https://doi.org/10.1017/aer.2021.106 Published online by Cambridge University Press

[2] Gomez, J.C. and Garcia, E. Morphing unmanned aerial vehicles, *Smart Mater. Struct.*, 2011, **20**, (10), p 103001.
[3] Jinsong, L. Jian, S. and Yanju, L. Application status and future prospect of smart materials and structures in morphing aircraft, *Acta Aeronautica Et Astronautica Sinica*, 2014, **35**, (1), pp 29–45.
[4] Yousefikoma, A. Applications of smart structures to aircraft for performance enhancement, *Canad. Aeronaut. Space J.*, 2003, **49**, (4), pp 163–172.
[5] Xu, D., Hui, Z., Liu, Y. and Chen, G. Morphing control of a new bionic morphing aircraft with deep reinforcement learning, *Aerospace Sci. Technol.*, 2019, **92**, (10), pp 232–243.
[6] Hajarian, A., Zakerzadeh, M.R. and Baghani, M. Design, analysis and testing of a smart morphing airfoil actuated by SMA wires, *Smart Mater. Struct.*, 2019, **28**, p 115043.
[7] Guerrero, J.E., Maestro, D. and Bottaro, A. Biomimetic spiroid winglets for lift and drag control, *Comptes rendus - Mécanique*, 2012, **340**, (1-2), pp 67–80.
[8] Raj, V.M., Shah, D.A. and Boomadevi, P. Preliminary investigation on the effects of folding wingtips on the aerodynamics characteristics of flexible aircraft, *Int. J. Ambient Energy*, 2019, 01430750, pp 1–18.
[9] Ostovan, Y., Akpolat, M.T. and Uzol, O. Experimental investigation of the effects of winglets on the tip vortex behavior of a model horizontal axis wind turbine using particle image velocimetry, *Sol. Energy Eng.*, 2019, **141**, (1), 011006.
[10] Wang, C., Khodaparast, H.H. and Friswell, M.I. Conceptual study of a morphing winglet based on unsymmetrical stiffness, *Aerospace Sci. Technol.*, 2016, **58**, (13), pp 546–558.
[11] Pecora, R., Magnifico, M., Amoroso, F. and Monaco, E. Multi-parametric flutter analysis of a morphing wing trailing edge, *Aeronaut. J. New Ser.*, 2014, **118**, (1207), pp 1063–1078.
[12] Eguea, J.P., Silva, G.P.G.D. and Catalano, F.M. Fuel efficiency improvement on a business jet using a camber morphing winglet concept, *Aerospace Sci. Technol.*, 2020, **96**, p 105542.
[13] Noviello, M.C., Dimino, I., Concilio, A., Amoroso, F. and Pecora, R. Aeroelastic assessments and functional hazard analysis of a regional aircraft equipped with morphing winglets, Aerospace, 2019, **6**, (104), 6100104, pp 1–19.
[14] Wang, C., Khodaparast, H.H. and Friswell, M.I. Conceptual study of a morphing winglet based on unsymmetrical stiffness, *Aerosp. Sci. Technol.*, 2016, **58**, pp 546–558.
[15] Bourdin, P., Gatto, A. and Friswell, M.I. Aircraft control via variable cant-angle winglets, *J. Aircr.*, 2008, **45**, (2), pp 414–423.
[16] Arena, M., Concilio, A. and Pecora, R. Aero-servo-elastic design of a morphing wing trailing edge system for enhanced cruise performance, *Aerospace Sci. Technol.*, 2019, **86**, pp 215–235.
[17] Dimino, I., Gallorini, F., Palmieri, M. and Pispola, G. Electromechanical actuation for morphing winglets, *Actuators*, 2019, **8**, (42), 18020042, pp 1–16.
[18] De Breuker, R., Abdalla, M. and Gürdal, Z. Design of morphing winglets with the inclusion of nonlinear aeroelastic effects, *Aeronaut. J.*, 2011, **115**, (1174), pp 713–728.
[19] Duan, L.W., Wu, Z.-H. and Xu, Z.-W. Identification research of the piezoelectric smart structure system of aircraft wing based on ARX model, *Piezoelectrics Acoustooptics*, 2008, **30**, (6), pp 760–762.
[20] Leylek, E., Manzo, J. and Garcia, E. A bat-wing aircraft using the smart joint mechanism, *Adv. Sci. Technol.*, 2009, **58**, (58), pp 41–46.
[21] Chen, Y., Sun, J., Liu, Y. and Leng, J. Experiment and analysis of fluidic flexible matrix composite (F2MC) tube, *J. Intell. Mater. Syst. Struct.*, 2012, **23**, (3), pp 279–290.
[22] Chen, Y., Sun, J., Liu, Y. and Leng, J. Variable stiffness property study on shape memory polymer composite tube, *Smart Mater. Struct.*, 2012, **21**, (9), 094021, pp 1–9.
[23] Chen, Y., Yin, W., Liu, Y. and Leng, J. Structural design and analysis of morphing skin embedded with pneumatic muscle fibers, *Smart Mater. Struct.*, 2011, **20**, (8), 085033, pp 1–8.
[24] Rudenko, A., Hanning, A., Monner, H.P. and Horst, P. Extremely deformation morphing leading edge: optimization, design and structure testing, *J. Intell. Mater. Syst. Struct.*, 2018, **29**, (5), pp 764–773.
[25] Ai, Q., Weaver, P.M. and Azarpeyvand, M. Design and mechanical testing of a variable stiffness morphing trailing edge flap, *J. Intell. Mater. Syst. Struct.*, 2018, **29**, (4), pp 669–683.
[26] Hassanalian, M., Quintana, A. and Abdelkefi, A. Morphing and growing Macro unmanned air vehicle: Sizing process and stability, *Aerosp. Sci. Technol.*, 2018, **78**, pp 130–146.
[27] Li, D., Liu, Q., Wu, Y. and Xiang, J. Design and analysis of a morphing drag rudder on the aerodynamics, structural deformation, and the required actuating moment, *J. Intell. Mater. Syst. Struct.*, 2018, **29**, (6), pp 1038–1049.
[28] Gibson, R.F. A review of recent research on mechanics of multifunctional composite materials and structures, *Compos. Struct.*, 2010, **92**, (12), pp 2793–2810.
[29] Jha, A.K. and Kudva, J.N. Morphing aircraft concepts, classifications, and challenges, Proceedings of SPIE - The International Society for Optical Engineering, 2004, pp 213–224.
[30] Bilgen, O., Butt, L.M., Day, S.R., Sossi, C.A., Weaver, J.P., Wolek, A., Meason, W.H. and Inman, D.J. A novel unmanned aircraft with solid-state control surfaces: Analysis and flight demonstration, *J. Intell. Mater. Syst. Struct.*, 2013, **24**, (2), pp 147–167.
[31] Han, M.-W., Rodrigue, H., Kim, H., Song, S.-H. and Ahn, S.-H. Shape memory alloy/glass fiber woven composite for soft morphing winglets of unmanned aerial vehicles, *Compos. Struct.*, 2016, **140**, pp 202–212.
[32] Giurgiutiu, V. Review of smart-materials actuation solutions for aeroelastic and vibration control, *J. Intell. Mater. Syst. Struct.*, 2000, **11**, (7), pp 525–544.
[33] Onur, B. and Michael, I.F. Piezoceramic composite actuators for a solid-state variable-camber wing, *J. Intell. Mater. Syst. Struct.*, 2014, **25**, (7), pp 806–817.

https://doi.org/10.1017/aer.2021.106 Published online by Cambridge University Press

[34] Syaifuddin, M., Park, H.C. and Goo, N.S. Design and evaluation of LIPCA-actuated flapping device, *J. Korean Soc. Aeronaut. Space Sci.*, 2005, **15**, pp 1225–1230.
[35] Sun, X., Dai, Q. and Bilgen, O. Design and simulation of Macro-Fiber composite based serrated Macro flap for wind turbine blade fatigue load reduction, *Mater. Res. Express*, 2018, **5**, (5), 055505, pp 1–14.
[36] Ramadan, K.S., Sameoto, D. and Evoy, S. A review of piezoelectric polymers as functional materials for electromechanical transducers, *Smart Mater. Struct.*, 2014, **23**, (3), pp 33001–33026.
[37] Lester, H.C. and Lefebvre, S. Piezoelectric actuator models for active sound and vibration control of cylinders, *J. Intell. Mater. Syst. Struct.*, 1993, **4**, (3), pp 295–306.
[38] Tzen, J.J., Jeng, S.L. and Chieng, W.H. Modeling of piezoelectric actuator for compensation and controller design, *Precis. Eng.*, 2003, **27**, (1), pp 70–86.
[39] Nguyen, N.T. and Truong, T.Q. A fully polymeric Macropump with piezoelectric actuator, *Sens. Actuators B*, 2004, **97**, (1), pp 137–143.
[40] Djahid, G. and Sergey, P. Winglet geometry impact on DLR-F4 aerodynamics and an analysis of a hyperbolic winglet concept, *Aerospace*, 2017, **4**, (4), p 60.
[41] Guerrero, J., Sanguineti, M. and Wittkowski, K. CFD study of the impact of variable cant angle winglets on total drag reduction, *Aerospace*, 2018, **5**, (4), 5040126, pp 1–18.
[42] Guerrero, J.E., Sanguineti M. and Wittkowski, K. Variable cant angle winglets for improvement of aircraft flight performance, *Meccanica*, 2020, **55**, (1), pp 1–31.

Cite this article: Chen X., Liu J. and Li Q. (2022). The smart morphing winglet driven by the piezoelectric Macro Fiber Composite actuator. *The Aeronautical Journal*, **126**, 830–847. https://doi.org/10.1017/aer.2021.106